

1 Vertical variation of optical properties of mixed Asian dust/pollution plumes
2 according to pathway of air mass transport over East Asia

3
4 S.-K. Shin^{1,a}, D. Müller^{2,b}, Chulkyu Lee³, K. H. Lee⁴, D. Shin^{5,*}, Y. J. Kim¹, Y. M. Noh^{6,*}
5
6

7 ¹School of Environmental Science and Engineering, Gwangju Institute of Science &
8 Technology, Gwangju, Republic of Korea

9 ²School of Physics, Astronomy and Mathematics, University of Hertfordshire,
10 Hertfordshire, United Kingdom

11 ³Korea Meteorological Administration, Seoul, Republic of Korea

12 ⁴Department of Atmospheric and Environmental Science, Gangneung-Wonju
13 National University, Gangneung, Republic of Korea

14 ⁵Air Quality Forecasting Centre, Climate and Air Quality Research Department,
15 National Institute of Environmental Research, Incheon, Republic of Korea

16 ⁶International Environmental Research Centre (IERC), Gwangju Institute of Science
17 & Technology, Gwangju, Republic of Korea

18 ^anow at Department of Atmospheric and Environmental Science, Gangneung-Wonju
19 National University, Gangneung, Republic of Korea

20 ^bformerly at School of Environmental Science and Engineering, Gwangju Institute of
21 Science & Technology, Gwangju, Republic of Korea
22
23
24
25
26
27
28
29
30
31
32
33
34

35 * Corresponding Author
36 Y. M. Noh
37 Tel) +82-62-715-3392
38 Fax) +82-62-715-3402
39 Email) nym@gist.ac.kr
40

41 **Abstract:**

42 We use five years (2009 – 2013) of multiwavelength Raman lidar measurements at Gwangju,
43 Korea (35.10° N, 126.53° E) for the identification of changes of optical properties of East
44 Asian dust in dependence of its transport path over China. Profiles of backscatter and
45 extinction coefficients, lidar ratios, and backscatter-related Ångström exponents (wavelength
46 pair 355/532nm) were measured at Gwangju. Linear particle depolarization ratios were used
47 to identify East Asian dust layers. We used backward trajectory modelling to identify the
48 pathway and the vertical position of dust-laden air masses over China during long-range
49 transport. Most cases of Asian dust events can be described by the emission of dust in desert
50 areas and subsequent transport over highly polluted regions of China. The Asian dust plumes
51 could be categorized into two classes according to the height above ground at which these
52 plumes were transported: (cases I) the dust layers passed over China at high altitude levels (>
53 3 km) until arrival over Gwangju, and (case II) the Asian dust layers were transported near
54 the surface and within the lower troposphere (< 3 km) over industrialized areas before they
55 arrived over Gwangju. We find that the optical characteristics of these mixed Asian dust
56 layers over Gwangju differ in dependence of their vertical position above ground over China
57 and the change of height above ground during transport. The mean linear particle
58 depolarization ratio was 0.21 ± 0.06 (at 532 nm), the mean lidar ratios were 52 ± 7 sr at 355 nm
59 and 53 ± 8 sr at 532 nm, and the mean Ångström exponent was 0.74 ± 0.31 for case I. In
60 contrast, plumes transported at lower altitudes (case II) showed low depolarization ratios
61 (0.13 ± 0.04 at 532 nm), and higher lidar ratio (63 ± 9 sr at 355 nm and 62 ± 8 sr at 532 nm) and
62 Ångström exponents (0.98 ± 0.51). These numbers show that the optical characteristics of
63 mixed Asian plumes are more similar to optical characteristics of urban pollution. We find a
64 decrease of the linear depolarization ratio of the mixed dust/pollution plume in dependence of
65 transport time if the pollution layer travelled over China at low heights, i.e., below
66 approximately 3 km above ground. In contrast we do not find such a trend if the dust plumes
67 travelled at heights above 3 km over China. We need a longer time series of lidar
68 measurements in order to determine in a quantitative way the change of optical properties of
69 dust with transport time.

70

71

72 **Key words:** lidar, Asian dust, optical properties, particle depolarization ratio, mixing, vertical
73 distribution, long-range transport

74 **1. Introduction**

75 Desert dust is the most abundant natural source of atmospheric particles over land. Its
76 light-absorption capacity is strong in the ultraviolet regions of the solar spectrum (Jacobson
77 2012). The light-absorption capacity depends on the proportions of Fe_2O_3 , Al_2O_3 , SiO_2 ,
78 CaCO_3 , $\text{MgCO}_3(\text{s})$, clays, and other substances. The transport patterns of dust over North
79 Africa and East Asia as well as the vertical distribution of dust change intra- and inter-
80 annually. Thus the influence of dust on the atmosphere's radiation balance is complex (Griggs
81 and Noguera, 2002; Mahowald et al., 2006; Durant et al., 2009). Central East Asia has large
82 desert regions. Asian dust particles that originate from the Taklamakan desert in west China
83 and the Gobi desert in Mongolia and northwest China (Figure. 1) influence the regional
84 climate over East Asia and can be found as far as the west coast of North America (Husar et
85 al., 2001; McKendry., 2001; Huang et al., 2008). East Asian dust is particularly complicated
86 as it usually travels over densely populated and highly industrialized areas of China before it
87 moves out over Pacific Ocean. During transport over East Asia dust mixes with pollutants
88 such as industrial soot, toxic material, and acidic gases (Sun et al., 2005).

89 Field campaigns, such as ACE-Asia (Huebert et al., 2003) and ADEC (Mikami et al.,
90 2006) significantly added to our knowledge of the radiative effects of Asian dust. Carrico et
91 al. (2003) and Yu et al. (2006) found differences of dust optical properties as the result of the
92 mixing of dust with anthropogenic pollution between source regions of dust and observation
93 sites downwind of its source regions. The mixing between Asian dust and industrial pollutant
94 particles has significant influence on the size distribution and the chemical composition of
95 aerosol plumes (Wang et al., 2007; Sun et al., 2010).

96 There exist few studies on the degree of mixing that occurs between dust and
97 pollution during transport, the effect of the direction of dust transport across China, and the
98 vertical distribution of Asian dust layers during long-range transport over China. There still is

99 a lack of understanding of how much of the mixing of dust with pollutants depends on the
100 vertical distribution of dust when it passes over source regions of anthropogenic pollution in
101 East Asia. One reason of our limited knowledge is that there are only few vertically-resolved,
102 long-term observations of pollution over East Asia.

103 LIDAR (LIght Detection And Ranging) is a powerful technique for measuring the
104 vertical distribution of atmospheric aerosols with high temporal and spatial resolution. In this
105 study we use Raman lidar data taken at Gwangju, South Korea, between 2009 and 2013. In
106 our study we focus specifically on lidar observations of Asian dust layers as they passed over
107 China. We use backward trajectory analysis with HYSPLIT (HYbrid Single Particle
108 Lagrangian Integrated Trajectory) (Draxler and Rolph, 2003) model to identify the transport
109 pathway and the vertical distribution of the Asian dust layers during long-range transport.

110 The main objective of this study is to investigate the variation of optical properties of
111 mixtures of Asian dust with anthropogenic pollution in dependence of the pathways and
112 vertical distributions of these mixed dust layers during long-range transport. In this
113 contribution we used the linear particle depolarization ratio to identify these dust layers. We
114 present vertically-resolved optical properties such as lidar ratio and Ångström exponent.

115 Section 2 presents the methods used in this study. Section 3 presents our results. We
116 discuss our results and summarize our findings in section 4.

117

118 **2. Methodology**

119 **2.1 GIST Multi-wavelength Raman lidar**

120 The lidar station, dubbed MRS.LEA (Multi-wavelength Raman Spectrometer Lidar
121 in East Asia) of the Gwangju Institute of Science and Technology (GIST) is located at 35.10°
122 N, 126.53° E in the west-south-western part of the Korean peninsula (Figure. 1).

123 A description of the lidar system is given by Noh et al. (2007, 2008). The light source

124 of the lidar is a pulsed Nd:YAG laser that emits light pulses at 355 nm, 532 nm, and 1064 nm.
125 The laser output power is 140, 154, and 640 mJ at the three emission wavelengths,
126 respectively. The pulse repetition rate is 10 Hz. We use a beam expander at 532 nm and 1064
127 nm in order to reduce the divergence of the emitted light. The receiver consists of a 14-inch
128 Schmidt-Cassegrain telescope. The signals collected by the receiver telescope are separated
129 according to wavelength with beam splitters and then transmitted to photomultiplier tubes
130 (PMT). Transient recorders with 12-bit analog-to-digital converters and 250-MHz photon
131 counters are used for processing the output signals of the PMTs. The system allows us to
132 retrieve vertical profiles of the particle backscatter coefficients at 355, 532, and 1064 nm, the
133 particle extinction coefficients at 355 and 532 nm, the linear particle depolarization ratio at
134 532 nm, the water-vapor mixing-ratio, and profiles of silicon-dioxide (Müller et al., 2010;
135 Tatarov et al., 2011). Profiles of silicon-dioxide (quartz) can be used as a proxy of the
136 concentration of mineral dust. In this contribution we use the signals needed for measuring
137 particle backscatter and extinction coefficients at 355 and 532 nm and the linear particle
138 depolarization ratio at 532 nm. The measurements were carried out at night time under cloud-
139 free conditions.

140 The profiles of particle backscatter coefficients (β_p) at 355 and 532 nm were
141 calculated with the Raman method (Ansmann et al., 1992b). The overlap effect which
142 describes the incomplete overlap between outgoing laser beam and field of view of the
143 receiver telescope is cancelled out for the case of profiles of the backscatter coefficient
144 because the ratios of two signals (elastic signals from particles and molecules and the
145 nitrogen Raman signals) are computed (Wandinger and Ansmann, 2002). In that way we can
146 retrieve vertical profiles of the backscatter coefficient to 400 m above ground. The vertical
147 profiles of the aerosol extinction coefficients (α_p) at 355 and 532 nm were derived with the
148 use of the nitrogen vibration Raman signals at 387 and 607 nm (Ansmann et al., 1990),

149 respectively. The aerosol extinction coefficients can be retrieved above 780 m and 540 m
150 above ground at the measurement wavelengths of 355 nm and 532 nm, respectively. We
151 derive particle extinction-to-backscatter ratios (lidar ratios, denoted as S in this contribution)
152 at 355 and 532 nm from the profiles of β_p and α_p . The lidar ratios can be used for aerosol
153 typing (Müller et al., 2007). Murayama et al., (2004) find values of $S = 48.6$ sr at 355 nm and
154 $S = 43.1$ sr at 532 in a well-isolated Gobi dust-laden layer observed above 4 km over Tokyo.
155 De Tomasi et al. (2003) report an S value less than 50 sr at 351 nm for a Saharan dust layer.
156 Values of S at 355 nm ranged between 50 sr and 80 sr for dust observed over Leipzig,
157 Germany (Mattis et al., 2002). In contrast, Ferrare et al. (2002) report a high value of 68 ± 12
158 sr of the lidar ratio at 355 nm. This high lidar ratio was associated with air masses advected
159 from urban/industrial areas. Omar et al. (2009) finds values of 65-70 sr for the lidar ratio at
160 532 nm. The numbers describe continental-polluted aerosols and polluted dust.

161 The backscatter-related Ångström exponent for the wavelength pair of 355/532 nm
162 (denoted as \mathring{A}_β) is computed, too. The backscatter-related Ångström exponent is a good
163 indicator of the size of particles. High values (>1) are typically observed for accumulation
164 mode particles such as fresh biomass-burning particles. Low values (~ 0) are observed for
165 coarse mode particles such as Saharan dust or Asian dust (Eck et al., 1999; Sakai et al., 2002,
166 Chen et al., 2007). The values of 0.2-0.3 are reported as the values of \mathring{A}_β for Saharan dust
167 (Murayama et al., 2002; Tesche et al., 2009). Chen et al. (2007) and Müller et al. (2010) find
168 values of 0.7-1.5 for \mathring{A}_β for a mixture of mineral dust with urban haze. Values of 0.8-1.4 for
169 \mathring{A}_β were found for heavily polluted continental aerosol layers (Franke et al., 2003).

170 The depolarization ratio is used as indicator of particle shape (Bohren and Huffman,
171 1983). High values of the depolarization ratio of 0.3 to 0.35 at 532 nm indicate nearly pure
172 dust (Sugimoto and Lee, 2006; Freudenthaler et al., 2009). For example, Freudenthaler et al.
173 (2009) report a value of $\delta_p = 0.31$ at 532 nm for Saharan dust observed during SAMUM 2006.

174 Lidar observations were carried out close to the Taklamakan desert (Iwasaka et al., 2003) and
175 the Gobi desert (Yi et al., 2014). We assume that these dust layers exhibit nearly pure dust
176 conditions as anthropogenic pollution sources in these isolated areas are sparse. Values of δ_p
177 are in the range of 0.3 to 0.35 at 532 nm (Iwasaka et al., 2003; Yi et al., 2014). Small values,
178 e.g., values from 0.08 to 0.1 usually are an indicator that dust is mixed with spherical
179 particles (Murayama et al., 2004; Chen et al., 2009; Tesche et al., 2009; Burton et al., 2013).
180 Anthropogenic aerosols normally are spherical with a small depolarization ratio (Murayama
181 et al., 2003). The degree of depolarization decreases as the sphericity of particles increases.
182 The depolarization ratio is dependent on the mixing ratio of dust with spherical particles. For
183 instance, Burton et al. (2013) report values of $\delta_p = 0.13-0.20$ and $0.03-0.07$ at 532 nm for
184 polluted dust and urban aerosol particles, respectively.

185 Parallel polarized and perpendicular polarized signals are measured at 532 nm. The
186 linear volume depolarization ratio (aerosols + molecules) δ is defined as

$$187 \quad \delta = \frac{P_{\perp}}{P_{\parallel} + P_{\perp}}. \quad (1)$$

188 P_{\perp} and P_{\parallel} denote the backscatter signal intensities that are polarized perpendicular
189 and parallel with respect to the plane of polarization of the emitted laser beam, respectively.
190 The δ can be also defined as P_{\perp}/P_{\parallel} (Cairo et al., 1999). We calculated the δ by using both
191 definitions and compared the difference between the derived values. The results from each
192 individual definition agree within the uncertainty of our depolarization ratio measurements
193 (Tesche et al., 2009; Shin et al., 2013).

194 The linear particle depolarization ratio δ_p differs from δ as it depends on the
195 concentration of particles in relation to the concentration of air molecules. In this contribution
196 we use the linear particle depolarization ratio (δ_p) according to the definition by Shimizu et al.
197 (2004):

198
$$\delta_p = \frac{\delta(z)R_B(z) - \delta_m}{R_B(z) - 1} \quad (2)$$

199 The term δ_m is the linear depolarization ratio of air molecules at the wavelength of
 200 the emitted laser wavelength. We used the value $\delta_m=0.0044$ (Behrendt and Nakamura, 2002).
 201 This value takes account of our interference filters which have a full width at half maximum
 202 of 1.0 nm. $R_B(z)$ is the backscatter ratio, expressed as $(\beta_p + \beta_m)/\beta_m$ at altitude z . β_m denotes the
 203 backscatter coefficient of atmospheric molecules. The calibration of the polarization channels
 204 was carried out by using rotating polarizers following the methodology explained by
 205 Freudenthaler et al. (2009).

206

207 **2.2 Dust Layer Identification**

208 We use the profiles of the linear particle depolarization ratio for the identification of
 209 the Asian dust layers. An example of how the Asian dust layer was determined is shown in
 210 Figure 2. The Asian dust plume reached Korea on 22 April 2012. Figure 2 shows the time-
 211 height cross section of the range-corrected backscatter signals and the linear volume
 212 depolarization ratio at 532 nm. Figure 2 also shows the mean profiles of δ and δ_p , S at 355
 213 and 532 nm, and \hat{A}_β for the measurement from 13:15 to 14:05 UTC.

214 Values of δ_p for individual aerosol types are reported in literature, e.g. δ_p for Asian
 215 dust particles varies from 0.08-0.35 (Murayama et al., 2004; Shimizu et al., 2004; Chen et al.,
 216 2009; Shin et al., 2013) at 532 nm. Asian dust generally mixes with pollution during long-
 217 range transport which leads to variable δ_p . Thus, this range of 0.08-0.35 likely describes
 218 mixtures of dust with anthropogenic pollution. For instance, Chen et al. (2009) uses 0.08 as
 219 threshold value to identify dust in pollution. Furthermore, optical properties may also change
 220 during long-range transport. Shimizu et al. (2004) define 0.1 as threshold value for the
 221 determination of polluted dust. In this study we used 0.08 as threshold value of δ_p to identify

222 dust.

223 In figure 2, the layer between 2.7 km 4.6 km (layer II) contains Asian dust particles
224 as suggested from the values of δ_p , which are higher than 0.16. The mean value of δ_p in the
225 layer between 1.2 km and 2.5 km (layer I) is 0.11 and thus also points to the presence of dust
226 particles though the concentration of dust particles compared to the concentration of particles
227 of anthropogenic pollution may be lower in layer I compared to layer II.

228 Other aerosol optical properties in layer I and layer II differ, too. The values of the S
229 in layer I are 64 ± 4 sr and 66 ± 4 sr at 355 and 532 nm, respectively. The values of the S in
230 layer II are as low 55 ± 4 sr and 55 ± 3 sr at 355 and 532 nm, respectively, see Fig. 2d. The
231 standard deviations were computed for the lidar ratios in each of the layers we could identify.

232 The values of \mathring{A}_β in layer I are ~ 0.93 and thus considerably higher than in layer II
233 where we find a value of ~ 0.42 . These numbers suggest that the concentration of small
234 particles is higher in layer I than in layer II, respectively that the mean size of particles in
235 layer I is smaller than the mean size of particles in layer II. Regarding the interpretation of the
236 numbers of \mathring{A}_β we need to keep in mind that the backscatter-related Ångström exponent not
237 only depends on particle size but also on the complex refractive index and particle shape. The
238 same holds true for the values of S . The different numbers thus could also result from
239 differences in particle shape and their absorption properties in these mixed Asian dust layers.

240

241 **2.3 Analysis of Backward Trajectories and Model Simulations of Pollution Emissions**

242 We used the HYSPLIT model (Draxler and Rolph, 2003) to generate 120 hours
243 backward trajectories for air parcels arriving above our lidar site. The trajectories describe the
244 different altitude levels in which dust was transported prior to the lidar observations. They
245 also allow us to trace back the origin of the dust layers and the transport path.

246 The Monitoring Atmospheric Composition and Climate (MACC) global air quality

247 service of the European Centre for Medium-Range Weather Forecasts (ECMWF) provides a
248 re-analysis of global atmospheric composition. The re-analysis assimilates satellite data, e.g.
249 total aerosol optical depth (AOD) which is provided by the Moderate Resolution Imaging
250 Spectroradiometer (MODIS), into a global model and data assimilation system to correct for
251 model departures from observational data (Bellouin et al., 2013; Inness et al., 2013). This re-
252 analysis provides fields of aerosols, namely mineral dust, black carbon, organic matter, and
253 sulphate, as well as chemically reactive gases, and greenhouse gases. We used the aerosol
254 AOD from the MACC re-analysis to determine the intensity of pollution (AOD) in densely
255 populated and industrialized regions along the transport path of the dust layers and to
256 investigate the influence of anthropogenic pollution particles on the variation of the optical
257 properties of Asian dust.

258

259 **3. Results and discussion**

260 We present data that cover the time from 2009-2013. During this time we observed
261 38 Asian dust layers on 32 days. These Asian dust layers were identified on the basis of the
262 linear particle depolarization ratio measurements as described in section 2.2. The vertical
263 profiles of the linear particle depolarization ratio allow us to determine the vertical
264 distribution of the Asian dust layers.

265 Figure 3 shows the frequency distribution of δ_p , S , and \dot{A}_β of Asian dust plumes
266 observed during the observation period. The average value of δ_p for all observed Asian dust
267 layers is 0.17 ± 0.02 . The average values of S are 57 ± 6 sr at 355 nm and 57 ± 7 sr at 532 nm.
268 The mean value of \dot{A}_β is 0.84 ± 0.37 . The optical properties of each individual Asian dust layer
269 vary over a wide range of values. We find values of 0.08-0.33 for δ_p , 38-83 sr for S at 355 nm,
270 41-73 sr for S at 532 nm, and 0.38-1.71 for \dot{A}_β . The maximum value of δ_p is 0.33 at 532 nm.
271 The minimum values of S at 355 nm and 532 nm are 38 sr and 41 sr, respectively. The

272 minimum value of \dot{A}_β is 0.38. This maximum value of δ_p and the minimum values of S at 355
273 nm and 532 nm and \dot{A}_β are similar to the values of optical properties for pure dust particles.
274 In contrast with these values, low values of δ_p and high values of S and \dot{A}_β are also measured.
275 We find that the minimum value of δ_p is 0.08 at 532 nm. The maximum values of S at 355
276 nm and 532 nm are 83 sr and 73 sr, respectively. The maximum value of \dot{A}_β is 1.71. These
277 values are remarkably different from the values of optical properties of pure dust.

278 We speculate that these differences of the values of the optical properties of dust
279 particles are caused by the effect of long-range transport during which dust mixes with
280 anthropogenic pollution or biomass burning smoke when passing over industrialized/densely
281 populated regions in China.

282

283 **3.1 Qualitative Analysis of the Variation of Optical Properties of Mixed-Dust in** 284 **Dependence of Pollution Levels**

285 We divided the dust layers into two episodes. The two episodes differ according to
286 the level of pollution emissions along the transport pathway of the dust plumes. The
287 separation of our measurements into these two episodes was done on the basis of the
288 distribution of aerosol optical depth (AOD) of anthropogenic pollution over China. The
289 Asian dust layers were classified as “more polluted”, i.e., “MP” Asian dust when the
290 modelled AOD of anthropogenic pollution on that day was higher than the average AOD
291 (modelled) of all 32 observation days considered in this study. In contrast, Asian dust layers
292 that passed over China during episodes of lower AOD, i.e., AOD was below the mean value
293 of modelled AOD of all 32 observation days, are denoted as “less polluted”, i.e., “LP” Asian
294 dust.

295 We used model results by MACC and backward trajectory analysis (see section 2.3)
296 for the interpretation of our lidar results as we do not have direct observations of pollution,

297 e.g. particle optical depth, lidar ratios, the linear particle depolarization ratios, and Ångström
298 exponents along the transport path of the pollution plumes. The reliability of inferring AOD
299 of pollution from MACC re-analysis is validated by comparing it to results from AERONET
300 sunphotometer measurements. MACC model is widely used to estimate AOD of pollution
301 (Bellouin et al., 2013; Cesnulyte et al., 2014).

302 Figure 4 shows the distribution of aerosol optical depth (AOD) at 550 nm for dust
303 and anthropogenic pollution on 10 April 2010 and 8 March 2013. These pollutants include
304 organic matter, black carbon, and sulphate aerosol. The pollution AOD was computed with
305 the MACC model using re-analysis data of ECMWF. The re-analysis data from the MACC
306 model can be downloaded at the web page of ECMWF
307 (<http://apps.ecmwf.int/datasets/data/macc-reanalysis/>). Fig. 4 shows that Asian dust particles
308 emitted from the Taklamakan and the Gobi desert were transported across China. The model
309 results of AOD of anthropogenic pollutants over China for 10 April 2010 are significantly
310 higher than the model results of AOD on 8 March 2013.

311 Figure 5 shows the scatter diagram of \mathring{A}_β and S at 355 nm and 532 nm versus δ_p in
312 dependence of the transport events denoted as MP and LP. The mean value of δ_p of the Asian
313 dust layers denoted as “LP” cases ranges between 0.08 (threshold value that we use to
314 identify dust) and 0.33. The corresponding values of \mathring{A}_β vary between 0.38 and 1.71. The
315 lidar ratios range between 38 sr and 83 sr at 355 nm and between 41 sr and 73 sr at 532 nm.
316 The negative correlation of δ_p with \mathring{A}_β indicates that the impact of the non-spherical particles
317 (Asian dust with high δ_p) on the backscattered light decreases with increasing \mathring{A}_β . Higher
318 values of \mathring{A}_β indicate a considerable concentration of anthropogenic pollution particles which
319 in turn results in lower values of δ_p , of the mixed dust/pollution plumes.

320 Lower values of δ_p are dominantly found in the domain where lidar ratios are above
321 60-70 sr, except for a few cases. Comparably high lidar ratios are associated with air masses

322 from urban/industrial areas (Noh et al., 2007; Müller et al., 2007; Burton et al., 2012). We
323 find high values of δ_p for lidar ratios of 57 ± 7 sr at 355 nm and 55 ± 7 sr at 532 nm.

324 With regard to the MP cases the mean δ_p varies from 0.08 to 0.30. The corresponding
325 values of \dot{A}_β vary between 0.42 and 1.56. The lidar ratios vary between 44 sr and 74 sr at
326 355 nm and between 48 sr and 72 sr at 532 nm, respectively.

327 Figure 5(d-f) shows a negative correlation of δ_p with \dot{A}_β and S at 355 nm and 532 nm.
328 The mean values of the LP and MP cases are summarized in table 1. The transport pathway of
329 dust over eastern China should influence the degree to which anthropogenic aerosols in the
330 industrial areas contribute to the change of optical properties of dust. However, we do not
331 find significant differences between the LP cases and MP cases. We assume that there is
332 another factor that influences the change of the optical properties of the dust layers we
333 observed.

334

335 **3.2 Influence of pathway and vertical distribution of anthropogenic pollution on optical** 336 **properties of Asian dust**

337 We classified the Asian dust plumes into 2 categories with regard to height above
338 ground when they passed over regions of anthropogenic emissions. We used 3 km height
339 above ground for the classification. The height of 3 km is reported as the planetary boundary
340 layer. Pollutants emitted at the surface predominantly stay in the planetary boundary layer
341 (Noh et al., 2007; Xie et al., 2015). We assume that height above ground influences how
342 much anthropogenic pollution may mix with the dust layers and thus changes the optical
343 properties of the dust layers. The vertical positions of the dust plumes above ground during
344 transport over China were inferred from the model results. We assume that the height of the
345 dust plumes above ground can be distinguished by HYSPLIT model results although the
346 results may have a certain error because of the spatial and temporal complexity of the

347 meteorological fields involved in the computations.

348 Figure 6 shows the transport pathway and the change of the vertical position of the
349 dust plumes during transport to our lidar site. It is clear that backward trajectories cannot
350 provide us with information on the concentration of dust and anthropogenic pollution in the
351 air masses prior to observation over Korea. Still, backward trajectories show if the air masses
352 originated from or nearby the desert regions, and whether the air masses passed over densely
353 populated/industrialized regions.

354 Case I includes those Asian dust plumes that passed over industrialized areas in
355 China at high altitude level ($> 3\text{km}$ height above ground) as shown in figure 6a. The Asian
356 dust plumes were classified as Case II when they were transported through the near
357 surface/lower troposphere ($< 3\text{km}$ height above ground) over industrialized areas in China,
358 i.e., longitude range between 110° E and 125° E ; the locations of industrialized and densely
359 populated regions in China are shown in figure 1.

360 The mean values of the linear particle depolarization ratios of the Asian dust plumes
361 we observed are lower compared to the linear particle depolarization ratios of pure dust
362 particles. For example, Freudenthaler et al. (2009) report a value of $\delta_p = 0.31$ at 532 nm for
363 pure Saharan dust observed during SAMUM 2006.

364 The values of δ_p and the corresponding values of \mathring{A}_β and S at 355 nm and 532 nm for
365 the cases I and II are also shown in figure 6. The corresponding mean values of the
366 parameters of these two cases are also summarized in table 1.

367 We find different clusters of the optical properties of the dust layers when we take
368 into consideration their vertical position during transport. The cases I show larger values of δ_p
369 compared to the depolarization ratios in cases II. On average, \mathring{A}_β of case I is smaller than \mathring{A}_β
370 of case II. The average values of δ_p and \mathring{A}_β are 0.21 ± 0.06 and 0.74 ± 0.31 , respectively, for
371 case I. In contrast, δ_p and \mathring{A}_β are 0.13 ± 0.04 and 0.98 ± 0.35 , respectively, for case II. The

372 lowest values of S at 355 nm and 532 nm are also measured for high values of δ_p (0.21 ± 0.06).
373 We find values of 52 ± 7 sr at 355 nm and 53 ± 8 sr at 532 nm, respectively, for case I.
374 Comparably high values of S were found for case II, i.e. 63 ± 9 sr at 355 nm and 62 ± 8 sr at
375 532 nm. In that case the value of δ_p is 0.13 ± 0.04 .

376 There are several previous studies that report on linear particle depolarization ratios
377 of polluted dust after long-range transport. According to these studies the observed dust
378 particles were partly/completely mixed with anthropogenic pollution (Sakai et al., 2002;
379 Müller et al., 2003; Shimizu et al., 2004; Chen et al., 2007). As a result of the mixing of dust
380 with anthropogenic pollution, the values of δ_p were lower than the values of pure dust, which
381 is estimated to be 0.3-0.35 (Murayama et al., 2004; Freudenthaler et al., 2009). Likewise, the
382 values of \hat{A}_β and S also differ compared to the values of \hat{A}_β and S of pure dust.

383 We assume that the dust particles carried more anthropogenic pollution in cases
384 where the air masses travelled near the surface. Consequently, the optical characteristics of
385 the dust/pollution layers of case II are dominated by the optical properties of anthropogenic
386 pollutants. In contrast, the optical properties of dust layers that travelled at high altitudes
387 (case I) are less influenced by urban/industrial pollutants. Thus, the optical properties of these
388 dust layers are more likely to be those of pure dust.

389 The Asian dust plumes were classified into 4 categories. We considered not only the
390 level of pollution emissions along the transport pathway, i.e., “MP” Asian dust and “LP”
391 Asian dust, but also the vertical position of the layers when they passed over polluted regions
392 of China (“below 3km” and “above 3km”). Figure 7 shows scatter diagrams of \hat{A}_β
393 (wavelength range 355/532 nm), and S at 355 nm and 532 nm versus δ_p at 532 nm in
394 dependence of the level of pollution emission and the vertical position. The corresponding
395 mean values of the optical parameters of those clusters are given in Table 1. We expect that
396 the optical properties of Asian dust change most if pollution levels (in terms of AOD) are

397 high, (MP Asian case) and when the corresponding air masses passed over industrialized area
398 of China at low altitude (below 3km height above ground). The mean values of δ_p at 532 nm
399 and \mathring{A}_β are 0.13 ± 0.04 and 1.09 ± 0.30 , respectively, for this case which is denoted as
400 “MP_below 3km”. The mean values of S are 61 ± 10 sr at 355 nm and 64 ± 7 sr at 532 nm.
401 However, these values of optical properties of dust for MP_below 3km are not significantly
402 different from the case of “LP_below 3km”. In that case the mean values of δ_p at 532 nm and
403 \mathring{A}_β are 0.13 ± 0.03 and 1.00 ± 0.38 , respectively. The mean values of S are 64 ± 9 sr at 355 nm and
404 62 ± 8 sr at 532 nm.

405 The values of optical properties between “MP” and “LP” at high altitude also do not
406 differ significantly. The mean values of δ_p at 532 nm, \mathring{A}_β , and S are 0.24 ± 0.05 , 0.58 ± 0.14 , and
407 53 ± 5 sr at 355 nm and 53 ± 2 sr at 532 nm, respectively, for the case “MP_above 3km”. The
408 highest values of δ_p and lowest values of \mathring{A}_β are found for this case.

409 In the case of “LP_above 3km” the mean values of δ_p at 532 nm and \mathring{A}_β are
410 0.21 ± 0.05 and 0.65 ± 0.20 , respectively. The mean values of S are 51 ± 8 sr at 355 nm and 49 ± 9 sr,
411 respectively. We believe that the changes in the optical properties of Asian dust depend on the
412 vertical position of the dust plume rather than the level of pollution emission during transport.

413 The clusters denoted as Case I and Case II were classified according to the altitude
414 (above ground) at which the dust-laden air masses passed over industrialized/populated
415 regions of China. The differences of the optical properties of the dust layers are shown in
416 figure 8. The corresponding values of the optical characteristics of the Asian dust layers at
417 each individual height are summarized in table 2. The difference of the optical characteristics
418 of East Asian dust layers that travelled in surface-near heights and at high altitudes is obvious.
419 The values of δ_p , \mathring{A}_β , and S are 0.12 ± 0.01 , 1.00 ± 0.43 , and 63 ± 7 sr at 355 nm and 64 ± 6 sr at
420 532 nm, respectively, when Asian dust passed over China below 1 km height above ground.
421 These values reflect the fact that the optical properties of the dust/pollution plumes are

422 dominated by the anthropogenic part of the particles in these plumes. Lower values of δ_p
423 represent the dominance of spherical particles, i.e. the presence of urban pollution. High
424 values of \hat{A}_p indicate that small particles dominate in the lower altitude level. The high lidar
425 ratio also indicates the presence of urban pollution which tends to be more light-absorbing
426 (Müller et al., 2007). In contrast, values for δ_p , \hat{A}_p , and S are 0.23 ± 0.04 , 0.60 ± 0.17 , and 50 ± 6
427 sr at 355 nm and 49 ± 5 sr at 532 nm, respectively, after the dust layers had passed over China
428 at high altitudes, i.e., above 3 km. These values more likely reflect the optical characteristic
429 of Asian dust particles that are less affected by the contribution of anthropogenic pollution.
430 The optical properties of Asian dust layer observed in our study reflect mixtures between
431 different aerosol types.

432 We notice that these variations of the optical properties of Asian dust layers may not
433 only result from external mixing. Hygroscopic growth, aging and deposition during transport,
434 and internal mixing might be also affect dust properties (Burton et al., 2014). The
435 interpretation of the mixing state of Asian dust is a challenging task. The mixing state
436 depends on many variables which are poorly known. Sugimoto et al. (2015) tried to identify
437 the mixing state of Asian dust (internal mixing or external mixing) by using analytical
438 relationships inferred from lidar observation. However, we will not go into details here. We
439 assume that most of the Asian dust observed in this study was externally mixed.

440 The altitude in which the Asian dust layers passed over China have significant
441 influence on their optical characteristics. In our study, we took 3 km above ground as
442 threshold value as we observed a notable change of optical properties of the dust/pollution
443 plumes if they travelled above or below 3 km height above ground. Pollution particles below
444 3 km could mix and interact with Asian dust particles (more influence). In contrast, we
445 assume that optical properties of dust particles above 3 km are not that much influenced by
446 anthropogenic pollution as the mixing of pollution into these heights is less intense.

447 We emphasize that this threshold value of 3 km is merely a best estimate which is
448 governed by the set of data we have at hand. We lack in additional information that would
449 allow us to refine our data analysis. For example a longer time series of lidar measurements,
450 (vertically resolved) observations of pollution transported over China, measurements under
451 much more variable meteorological conditions, additional modelling results, just to name a
452 few reasons, might change this threshold value.

453 We also investigated the optical properties of Asian dust with respect to transport
454 time at different height level. Figure 9 shows scatter diagrams of optical properties of Asian
455 dust versus the transport time. The correlation study is based on HYSPLIT model results, our
456 profiles of δ_p , \dot{A}_p , and S , and the time (in hours) the Asian dust spent in polluted regions over
457 China during the transport. We can only use HYSPLIT results as an estimate of the total
458 transport time and the time the plumes spent over pollution regions of China. The total
459 transport time may have considerable uncertainty. We need to decide from the trajectories the
460 start point of dust emission and this means we take the time when the air parcel (defined by
461 its trajectory) left one of the desert regions in Central Asia. The height above ground during
462 transport and the time the plumes spent over pollution regions also contains uncertainty as we
463 neither have direct measurements of the height distribution of the plumes over China during
464 transport nor do we have information on the pollution levels over China while the desert
465 plumes travelled over China in the various height layers. We can merely assume that the
466 likelihood of mixing with dust and pollution increases the lower the dust travels above
467 ground and the longer it travels at low heights.

468 We again used our classification of Case I and Case II. However, we refined the
469 vertical resolution to 5 height layers, i.e. transport occurred below 1 km, from 1-2 km, from
470 2-3 km, from 3-4 km, and above 4 km. We wanted to test if a more refined height separation
471 would give us more insight on the change of optical properties with transport time and

472 transport height.

473 The absolute time the dust layers spent in these different height levels is presented in
474 figure 9. We also tested the effect of relative time in relation to total transport time but could
475 not find a clear pattern. We find a maximum value of 0.3 for δ_p at 532 nm. On average, the
476 depolarization decreases with increasing residence time over China. However, this
477 dependence differs with respect to the height above ground of dust layers. The change of the
478 depolarization ratio of dust layers travelling above 3 km above ground seems less dependent
479 on the residence time over a given area.

480 We believe that short residence times (fast transport to Korea, 20 hours or less)
481 reduces the chances that pollution may mix with dust, particularly if dust travelled below 3
482 km above ground. In contrast, longer residence times (slow transport to Korea, >50 hours) of
483 the dust plumes may have increased the chances that pollution mixed with dust if dust
484 travelled below 3km height above ground.

485 Regarding \dot{A}_β we find a maximum value of 1.75 which decreases to 0.5 for slow
486 transport of the plumes. The decrease of \dot{A}_β with transport time seems to be correlated for
487 plumes that mainly stay below 3 km height above ground. In contrast, if plumes were above 3
488 km, \dot{A}_β does not seem to change with transport time. In that case, the mixing of pollution with
489 dust may have been less likely because of the fast transport.

490 With regard to S at 355 nm and 532 nm we find a maximum value of approximately
491 75 sr which drops to approximately 40 sr for slow transport. Again, we see that for plumes
492 below 3 km height above ground transport time seems to matter. S drops with increasing
493 transport time. For the case of plumes above 3 km, i.e. dust that likely is not too much
494 affected by mixing with anthropogenic pollution, the lidar ratios do not seem to depend on
495 transport time. This result may however again be caused by the fact that transport times to
496 Korea are comparably short.

497 We further investigated these results. We initially assumed that \mathring{A}_β either should
498 increase with transport time or does not drop significantly for pollution that travels near the
499 ground as there should be a higher share of small anthropogenic pollution particles in the dust
500 plume (large particles). This opposite behaviour may be caused by the state of mixing, i.e.,
501 pollution particles attach to the dust particles, thus increasing their mean size. Hygroscopic
502 growth of particles attached to dust may further contribute to the increase of mean size. One
503 point that complicates this interpretation is that \mathring{A}_β does not only depend on particle size but
504 also on particle shape and the real and imaginary part (scattering and absorption) of the
505 particles.

506 With regard to S we also expected that S would increase with increasing transport
507 times. If the particles travel at low height above ground more anthropogenic pollution should
508 mix with dust. The decrease of S however suggests an increase of particle size and a decrease
509 of the light-absorption capacity. Hygroscopic particle growth, i.e. increase of mean particle
510 size and decrease of light-absorption by uptake of water might be responsible for this
511 behavior.

512 We stress that other reasons may be responsible for these results. We have a
513 comparably small set of observations. We have insufficient information whether the plumes
514 consisted of internal and/or external mixtures. The shape and size of particles of mixed Asian
515 dust might be influenced in a much more significant way by transport time. The kind of
516 mixing between the dust particles and pollution particles could influence the light-absorption
517 properties.

518

519 **4. Summary and Conclusion**

520 In this study we presented the differences of optical properties of mixed Asian dust
521 layers in dependence of their vertical position over China during transport from the Chinese

522 dust source regions to Korea, downwind region of the source regions. The data cover the time
523 frame from 2009-2013. The dust layers are divided into several categories which can be
524 characterized by different heights above ground during transport. The change of height above
525 ground during transport of the dust layers was identified by backward trajectory analysis.

526 The optical properties of Asian dust significantly change in dependence of the dust
527 plumes, the vertical position, and the change of vertical position above ground level during
528 transport over China. We find lower values of the lidar ratios at 355 and 532 nm, lower
529 backscatter-related Ångström exponents (wavelength pair 355/532 nm), and higher linear
530 particle depolarization ratios at 532 nm for Asian dust that was transported at high altitudes
531 (> 3km height above ground) compared to the situation in which the dust plumes moved at
532 low altitudes across China. The mean linear particle depolarization ratio is 0.21 ± 0.06 for
533 transport at high altitudes. The mean lidar ratios in that case are 52 ± 7 sr and 53 ± 8 sr at 355
534 nm and 532 nm, respectively. The mean Ångström exponent is 0.74 ± 0.31 . These values likely
535 reflect properties of dust little affected by anthropogenic pollution. However, we cannot
536 quantify the amount of anthropogenic pollution that may still be present in these dust layers.
537 In contrast, higher values of the lidar ratios and the backscatter-related Ångström exponents,
538 and lower values of the linear particle depolarization were found for dust layers that crossed
539 highly polluted regions in China at low altitudes. The value of the mean linear particle
540 depolarization ratio is 0.13 ± 0.04 . The mean lidar ratios are 63 ± 9 sr and 62 ± 8 sr at 355 nm
541 and 532 nm, respectively. The mean backscatter-related Ångström exponent is 0.98 ± 0.35 .
542 These values more likely describe strong influence by anthropogenic pollution, i.e. the uptake
543 of urban pollution by dust may have been significant.

544 Our results suggest that the transport pathway as well as the vertical position of Asian
545 dust during long-range transport may have significant impact on the optical properties of
546 mixed Asian dust layers.

547 **Acknowledgements**

548
549 This work was supported by a National Research Foundation of Korea (NRF) grant funded
550 by the Korean government (MEST) (No. 2012R1A1A2002983). This work was also
551 supported by the Korea Meteorological Administration Research and Development Program
552 under grant KMIPA2015-2012.

553
554
555
556
557
558
559
560
561
562
563
564
565
566
567
568
569
570
571
572
573
574
575
576
577
578
579
580
581
582
583
584
585
586
587
588
589
590
591

592 **References**

593
594
595
596
597
598
599
600
601
602
603
604
605
606
607
608
609
610
611
612
613
614
615
616
617
618
619
620
621
622
623
624
625
626
627
628
629
630
631
632
633
634
635
636
637
638
639
640

Anderson, T. L., Masonis, S. J., Covert, D. S., Charlson, R. J., and Rood, M. J.: In situ measurement of the aerosol extinction-to-backscatter ratio at a polluted continental site, *Journal of Geophysical Research: Atmospheres* (1984–2012), 105, 26907-26915, 2000.

Ansmann, A., Riebesell, M., Wandinger, U., Weitkamp, C., Voss, E., Lahmann, W., and Michaelis, W.: Combined Raman elastic-backscatter lidar for vertical profiling of moisture, aerosol extinction, backscatter, and lidar ratio, *Applied Physics B*, 55, 18-28, 1992a.

Ansmann, A., Riebesell, M., and Weitkamp, C.: Measurement of atmospheric aerosol extinction profiles with a Raman lidar, *Optics Letters*, 15, 746-748, 1990.

Ansmann, A., Wandinger, U., Riebesell, M., Weitkamp, C., and Michaelis, W.: Independent measurement of extinction and backscatter profiles in cirrus clouds by using a combined Raman elastic-backscatter lidar, *Applied Optics*, 31, 7113-7131, 1992b.

Behrendt, A., and Nakamura, T.: Calculation of the calibration constant of polarization lidar and its dependency on atmospheric temperature, *Optics express*, 10, 805-817, 2002.

Bellouin, N., Quaas, J., Morcrette, J.-J., and Boucher, O.: Estimates of aerosol radiative forcing from the MACC re-analysis, *Atmospheric Chemistry and Physics*, 13, 2045-2062, 2013.

Bohren, C. F., and Huffman, D. R.: *Absorption and scattering by a sphere*, *Absorption and Scattering of Light by Small Particles*, 82-129, 1983.

Burton, S., Ferrare, R., Hostetler, C., Hair, J., Rogers, R., Obland, M., Butler, C., Cook, A., Harper, D., and Froyd, K.: Aerosol classification using airborne High Spectral Resolution Lidar measurements—methodology and examples, *Atmospheric Measurement Techniques*, 5, 73-98, 2012.

Burton, S., Ferrare, R., Vaughan, M., Omar, A., Rogers, R., Hostetler, C., and Hair, J.: Aerosol classification from airborne HSRL and comparisons with the CALIPSO vertical feature mask, *Atmospheric Measurement Techniques*, 6, 1397-1412, 2013.

Burton, S., Vaughan, M., Ferrare, R., Hostetler, C.: Separating mixtures of aerosol types in airborne High Spectral Resolution Lidar data, *Atmospheric Measurement Techniques*, 7, 419-436, 2014.

Cairo, F., Di Donfrancesco, G., Adriani, A., Pulvirenti, L., and Fierli, F.: Comparison of various linear depolarization parameters measured by lidar, *Applied Optics*, 38, 4425-4432, 1999.

Carrico, C. M., Kus, P., Rood, M. J., Quinn, P. K., and Bates, T. S.: Mixtures of pollution, dust, sea salt, and volcanic aerosol during ACE-Asia: radiative properties as a function of relative humidity, *J. Geophys. Res.-Atmos.*, 108(D23), 8650, doi: 10.1029/2003JD003405, 2003.

641 Cattrall, C., Reagan, J., Thome, K., and Dubovik, O.: Variability of aerosol and spectral lidar
642 and backscatter and extinction ratios of key aerosol types derived from selected Aerosol
643 Robotic Network locations, *Journal of Geophysical Research: Atmospheres* (1984–2012),
644 110, doi: 10.1029/2004JD005124, 2005.

645
646 Cesnulyte, V., Lindfors, A., Pitkänen, M., Lehtinen, K., Morcrette, J.-J., and Arola, A.:
647 Comparing ECMWF AOD with AERONET observations at visible and UV wavelengths,
648 *Atmospheric Chemistry and Physics*, 14, 593-608, 2014.

649
650 Chen, W.-N., Chen, Y.-W., Chou, C. C., Chang, S.-Y., Lin, P.-H., and Chen, J.-P.: Columnar
651 optical properties of tropospheric aerosol by combined lidar and sunphotometer
652 measurements at Taipei, Taiwan, *Atmospheric Environment*, 43, 2700-2708, 2009.

653
654 Chen, W.-N., Tsai, F.-J., Chou, C. C.-K., Chang, S.-Y., Chen, Y.-W., and Chen, J.-P.: Optical
655 properties of Asian dusts in the free atmosphere measured by Raman lidar at Taipei, Taiwan,
656 *Atmospheric Environment*, 41, 7698-7714, 2007.

657
658 De Tomasi, F., Blanco, A., and Perrone, M. R.: Raman lidar monitoring of extinction and
659 backscattering of African dust layers and dust characterization, *Applied Optics*, 42, 1699-
660 1709, 2003.

661
662 Draxler, R. R. and Rolph, G.: HYSPLIT (Hybrid Single-Particle Lagrangian Integrated
663 Trajectory) model access via NOAA ARL READY website, NOAA Air Resources
664 Laboratory, Silver Spring, MD, available at: <http://www.arl.noaa.gov/ready/hysplit4.html>
665 (last access: October 2014), 2003.

666
667 Durant, A. J., Harrison, S. P., Watson, I. M., and Balkanski, Y.: Sensitivity of direct radiative
668 forcing by mineral dust to particle characteristics, *Progress in Physical Geography*, 33, 80-
669 102, 2009.

670
671 Eck, T., Holben, B., Reid, J., Dubovik, O., Smirnov, A., O'Neill, N., Slutsker, I., and Kinne,
672 S.: Wavelength dependence of the optical depth of biomass burning, urban, and desert dust
673 aerosols, *Journal of Geophysical Research: Atmospheres* (1984–2012), 104, 31333-31349,
674 1999.

675
676 Ferrare, R. A., Turner, D. D., Brasseur, L. H., Feltz, W. F., Dubovik, O., and Tooman, T. P.:
677 Raman lidar measurements of the aerosol extinction-to-backscatter ratio over the Southern
678 Great Plains, *Journal of Geophysical Research: Atmospheres* (1984–2012), 106, 20333-
679 20347, doi:10.1029/2000JD000144, 2001.

680
681 Franke, K., Ansmann, A., Müller, D., Althausen, D., Venkataraman, C., Reddy, M. S.,
682 Wagner, F., and Scheele, R.: Optical properties of the Indo-Asian haze layer over the tropical
683 Indian Ocean, *Journal of Geophysical Research: Atmospheres* (1984–2012), doi:
684 10.1029/2002JD002473, 108, 2003.

685
686 Freudenthaler, V., Esselborn, M., Wiegner, M., Heese, B., Tesche, M., Ansmann, A., Müller,
687 D., Althausen, D., Wirth, M., and Fix, A.: Depolarization ratio profiling at several
688 wavelengths in pure Saharan dust during SAMUM 2006, *Tellus B*, 61, 165-179, 2009.

689

690 Griggs, D. J., and Noguera, M.: Climate change 2001: the scientific basis. Contribution of
691 working group I to the third assessment report of the intergovernmental panel on climate
692 change, *Weather*, 57, 267-269, 2002.

693

694 Huang, J., Minnis, P., Chen, B., Huang, Z., Liu, Z., Zhao, Q., Yi, Y., and Ayers, J. K.: Long-
695 range transport and vertical structure of Asian dust from CALIPSO and surface
696 measurements during PACDEX, *J. Geophys. Res.-Atmos.*, 113(D23), D23212, doi:
697 10.1029/2008JD010620, 2008.

698 Huebert, B. J., Bates, T., Russell, P. B., Shi, G., Kim, Y. J., Kawamura, K., Carmichael, G.,
699 and Nakajima, T.: An overview of ACE-Asia: strategies for quantifying the relationships
700 between Asian aerosols and their climatic impacts, *J. Geophys. Res.-Atmos.*, 108(D23), 8633,
701 doi: 10.1029/2003JD003550, 2003.

702

703 Husar, R. B., Tratt, D., Schichtel, B. A., Falke, S., Li, F., Jaffe, D., Gasso, S., Gill, T.,
704 Laulainen, N. S., and Lu, F.: Asian dust events of April 1998, *Journal of Geophysical
705 Research: Atmospheres (1984–2012)*, 106, 18317-18330, 2001.

706

707 Inness, A., Baier, F., Benedetti, A., Bouarar, I., Chabrilat, S., Clark, H., Clerbaux, C.,
708 Coheur, P., Engelen, R., and Errera, Q.: The MACC reanalysis: an 8 yr data set of
709 atmospheric composition, *Atmos Chem Phys*, 13, 4073-4109, 2013.

710

711 Iwasaka, Y., Shibata, T., Nagatani, T., Shi, G. Y., Kim, Y., Matsuki, A., Trochkin, D.,
712 Zhang, D., Yamada, M., and Nagatani, M.: Large depolarization ratio of free tropospheric
713 aerosols over the Taklamakan Desert revealed by lidar measurements: Possible diffusion and
714 transport of dust particles, *J. Geophys. Res.-Atmos.*, 108(D23), 8652, doi:
715 10.1029/2002JD003267, 2003.

716

717 Jacobson, M. Z.: Investigating cloud absorption effects: Global absorption properties of black
718 carbon, tar balls, and soil dust in clouds and aerosols, *Journal of Geophysical Research:
719 Atmospheres (1984–2012)*, 117, D06205, doi: 10.1029/2011JD017218, 2012

720

721 Mahowald, N. M., Muhs, D. R., Levis, S., Rasch, P. J., Yoshioka, M., Zender, C. S., and Luo,
722 C.: Change in atmospheric mineral aerosols in response to climate: last glacial period,
723 preindustrial, modern, and doubled carbon dioxide climates, *J. Geophys. Res.-Atmos.*,
724 111(D10), D10202, doi: 10.1029/2005JD006653, 2006.

725

726 Mattis, I., Ansmann, A., Müller, D., Wandinger, U., and Althausen, D.: Dual-wavelength
727 Raman lidar observations of the extinction-to-backscatter ratio of Saharan dust, *Geophysical
728 Research Letters*, 29, 20-21-20-24, 2002.

729

730 McKendry, I., Hacker, J., Stull, R., Sakiyama, S., Mignacca, D., and Reid, K.: Long-range
731 transport of Asian dust to the Lower Fraser Valley, British Columbia, Canada, *Journal of
732 Geophysical Research: Atmospheres (1984–2012)*, 106, 18361-18370, 2001.

733

734 Mikami, M., Shi, G., Uno, I., Yabuki, S., Iwasaka, Y., Yasui, M., Aoki, T., Tanaka, T.,
735 Kurosaki, Y., and Masuda, K.: Aeolian dust experiment on climate impact: An overview of
736 Japan–China joint project ADEC, *Global and Planetary Change*, 52, 142-172, 2006.

737

738 Müller, D., Ansmann, A., Mattis, I., Tesche, M., Wandinger, U., Althausen, D., and Pisani,

739 G.: Aerosol-type-dependent lidar ratios observed with Raman lidar, *J. Geophys. Res.-*
740 *Atmos.*,112(D16), D16202, doi: 10.1029/2006JD008292, 2007.

741

742 Müller, D., Franke, K., Ansmann, A., Althausen, D., and Wagner, F.: Indo-Asian pollution
743 during INDOEX: microphysical particle properties and single-scattering albedo inferred from
744 multiwavelength lidar observations, *J. Geophys. Res.-Atmos.*, 108(D19), 4600, doi:
745 10.1029/2003JD003538, 2003.

746

747 Müller, D., Mattis, I., Tatarov, B., Noh, Y., Shin, D., Shin, S., Lee, K., Kim, Y., and
748 Sugimoto, N.: Mineral quartz concentration measurements of mixed mineral dust/urban haze
749 pollution plumes over Korea with multiwavelength aerosol Raman-quartz lidar, *Geophys.*
750 *Res. Lett.*, 37(20), L20810, doi: 10.1029/2010GL044633, 2010.

751

752 Murayama, T., Masonis, S. J., Redemann, J., Anderson, T. L., Schmid, B., Livingston, J. M.,
753 Russell, P. B., Huebert, B., Howell, S. G., and McNaughton, C. S.: An intercomparison of
754 lidar-derived aerosol optical properties with airborne measurements near Tokyo during
755 ACE-Asia, *Journal of Geophysical Research: Atmospheres* (1984–2012), 108, doi:
756 10.1029/2002JD003259, 2003.

757

758 Murayama, T., Müller, D., Wada, K., Shimizu, A., Sekiguchi, M., and Tsukamoto, T.:
759 Characterization of Asian dust and Siberian smoke with multi-wavelength Raman lidar over
760 Tokyo, Japan in spring 2003, *Geophys. Res. Lett.*, 31(23), L23103, doi:
761 10.1029/2004GL021105, 2004.

762

763 Murayama, T.: Optical properties of Asian dust aerosol lofted over Tokyo observed by
764 Raman lidar, *Lidar Remote Sensing in Atmospheric and Earth Sciences*, edited by
765 Bissonnette, LR, Roy, G., and Vallée, G., Defence R&D Canada, Val-Bélair, 1, 331-334,
766 2002.

767

768 Noh, Y. M., Kim, Y. J., Choi, B. C., and Murayama, T.: Aerosol lidar ratio characteristics
769 measured by a multi-wavelength Raman lidar system at Anmyeon Island, Korea,
770 *Atmospheric Research*, 86, 76-87, 2007.

771

772 Noh, Y. M., Kim, Y. J., and Müller, D.: Seasonal characteristics of lidar ratios measured with
773 a Raman lidar at Gwangju, Korea in spring and autumn, *Atmospheric Environment*, 42,
774 2208-2224, 2008.

775

776 Omar, A. H., Winker, D. M., Vaughan, M. A., Hu, Y., Trepte, C. R., Ferrare, R. A., Lee, K.-
777 P., Hostetler, C. A., Kittaka, C., and Rogers, R. R.: The CALIPSO automated aerosol
778 classification and lidar ratio selection algorithm, *Journal of Atmospheric and Oceanic*
779 *Technology*, 26, 1994-2014, 2009.

780

781 Sakai, T., Shibata, T., Iwasaka, Y., Nagai, T., Nakazato, M., Matsumura, T., Ichiki, A., Kim,
782 Y.-S., Tamura, K., and Troshkin, D.: Case study of Raman lidar measurements of Asian dust
783 events in 2000 and 2001 at Nagoya and Tsukuba, Japan, *Atmospheric Environment*, 36,
784 5479-5489, 2002.

785

786 Shimizu, A., Sugimoto, N., Matsui, I., Arao, K., Uno, I., Murayama, T., Kagawa, N., Aoki,
787 K., Uchiyama, A., and Yamazaki, A.: Continuous observations of Asian dust and other

788 aerosols by polarization lidars in China and Japan during ACE-Asia, *J. Geophys. Res.-*
789 *Atmos.*, 109(D19), D19S17, doi: 10.1029/2002JD003253, 2004.

790

791 Shin, S., Müller, D., Kim, Y., Tatarov, B., Shin, D., Seifert, P., and Noh, Y. M.: The retrieval
792 of the Asian dust depolarization ratio in Korea with the correction of the polarization-
793 dependent transmission, *Asia-Pacific Journal of Atmospheric Sciences*, 49, 19-25, 2013.

794

795 Sugimoto, N., and Lee, C. H.: Characteristics of dust aerosols inferred from lidar
796 depolarization measurements at two wavelengths, *Applied Optics*, 45, 7468-7474, 2006.

797

798 Sugimoto, N., Nishizawa, T., Shimizu, A., Matsui, I., and Kobayashi, H.: Detection of
799 internally mixed Asian dust with air pollution aerosols using a polarization optical particle
800 counter and a polarization-sensitive two-wavelength lidar, *Journal of Quantitative*
801 *Spectroscopy and Radiative Transfer*, 150, 107-113, 2015.

802

803 Sun, Y., Zhuang, G., Huang, K., Li, J., Wang, Q., Wang, Y., Lin, Y., Fu, J. S., Zhang, W.,
804 and Tang, A.: Asian dust over northern China and its impact on the downstream aerosol
805 chemistry in 2004, *J. Geophys. Res.-Atmos.*, 115(D17), D00K09, doi:
806 10.1029/2009JD012757, 2010.

807

808 Sun, Y., Zhuang, G., Wang, Y., Zhao, X., Li, J., Wang, Z., and An, Z.: Chemical composition
809 of dust storms in Beijing and implications for the mixing of mineral aerosol with pollution
810 aerosol on the pathway, *J. Geophys. Res.-Atmos.*, 110(D24), D24209, doi:
811 10.1029/2005JD006054, 2005.

812

813 Tatarov, B., Müller, D., Shin, D. H., Shin, S. K., Mattis, I., Seifert, P., Noh, Y. M., Kim, Y.,
814 and Sugimoto, N.: Lidar measurements of Raman scattering at ultraviolet wavelength from
815 mineral dust over East Asia, *Optics express*, 19, 1569-1581, 2011.

816

817 Tesche, M., Ansmann, A., Müller, D., Althausen, D., Engelmann, R., Freudenthaler, V., and
818 Groß, S.: Vertically resolved separation of dust and smoke over Cape Verde using
819 multiwavelength Raman and polarization lidars during Saharan Mineral Dust Experiment
820 2008, *Journal of Geophysical Research: Atmospheres* (1984–2012), 114,
821 doi:10.1029/2009JD011862, 2009.

822

823 Tesche, M., Ansmann, A., Müller, D., Althausen, D., Mattis, I., Heese, B., Freudenthaler, V.,
824 Wiegner, M., Esselborn, M., and Pisani, G.: Vertical profiling of Saharan dust with Raman
825 lidars and airborne HSRL in southern Morocco during SAMUM, *Tellus B*, 61, 144-164, 2009.

826

827 Wandinger, U., and Ansmann, A.: Experimental determination of the lidar overlap profile
828 with Raman lidar, *Applied Optics*, 41, 511-514, 2002.

829

830 Wang, Y., Zhuang, G., Tang, A., Zhang, W., Sun, Y., Wang, Z., and An, Z.: The evolution of
831 chemical components of aerosols at five monitoring sites of China during dust storms,
832 *Atmospheric Environment*, 41, 1091-1106, 2007.

833

834 Xie, C., Zhao, M., Wang, B., Zhong, Z., Wang, L., Liu, D., and Wang, Y.: Study of the
835 scanning lidar on the atmospheric detection, *Journal of Quantitative Spectroscopy and*
836 *Radiative Transfer*, 150, 114-120, 2015.

837
838
839
840
841
842
843
844

845

846

847

848

849

850

851

852

853

854

855

856

857

858

859

860

861

862

863

864

Yi, B., Yang, P., and Baum, B. A.: Impact of pollution on the optical properties of trans-Pacific East Asian dust from satellite and ground-based measurements, *J. Geophys. Res. Atmos.*, 119(9), 5397-5409, doi: 10.1002/2014JD021721, 2014.

Yu, X., Cheng, T., Chen, J., and Liu, Y.: A comparison of dust properties between China continent and Korea, Japan in East Asia, *Atmospheric Environment*, 40, 5787-5797, 2006.

865 Table captions

866

867 Table 1. Summary of the linear particle depolarization ratio at 532 nm, lidar ratios, and backscatter-
868 related Ångström exponents of Asian dust layers for each classification. Asian dust layers were
869 classified according to (a) levels of anthropogenic pollution emission; LP denotes that Asian dust
870 layers which are considered as less polluted and MP denotes that Asian dust layers which are
871 considered as more polluted, (b) their vertical position at polluted region; Case I indicates Asian dust
872 layers passed over China at high altitude (> 3 km) before they arrived over Gwangju, and Case II
873 indicates Asian dust layers were transported at low altitude (< 3 km) over industrialized areas before
874 they arrived over Gwangju, and (c) their vertical position (below 3 km or above 3 km) and level of
875 pollution (LP or MP) when they passed over China

876

877 Table 2. Linear particle depolarization ratio at 532 nm, lidar ratios, and backscatter-related
878 Ångström exponents of East Asian dust layers according to altitude range in which these plumes
879 passed over polluted regions of China. Case I describes the layer from 3-4 km and above 4 km. Case
880 II describes the layers from 0-1 km, from 1-2 km, and from 2-3 km height above ground.

881

882

883

884

885

886

887

888

889

890

891

892

893

894

895

896

897

898 Figure captions

899

900 Figure 1. Map of the desert regions (Taklimakan desert, Gobi desert, Badain Jaran desert, Ordos
901 Desert, Inner Mongolia plateau, and Manchuria) and loess regions (Loess Plateau and Manchuria).
902 The location of some major cities (Beijing and Shanghai) and industrialized areas of China (Hebei,
903 Shandong, Henan, and Zhejiang province) is also shown. MRS.LEA is located in Gwangju, Korea.
904

905 Figure 2. Measurement on 22 April 2012, 13:15-14:05 UTC. Shown are (a) the time-height cross
906 section of the range-corrected signal and (b) the volume depolarization ratio at 532 nm. Also shown
907 are the profiles of (c) the volume depolarization ratio and the linear particle depolarization ratio at 532
908 nm, and (d) the lidar ratio at 355 and 532 nm and the backscatter-related Ångström exponents.
909

910 Figure 3. Frequency distributions of optical properties of Asian dust observed between 2009 and 2013.
911 Shown are (a,b) lidar ratios at 355 and 532 nm, (c) linear particle depolarization ratios at 532 nm, and
912 (d) Ångström exponents for the wavelength pair 355/532 nm. The numbers in each plot indicate the
913 mean value and its standard deviation, the median (shown in brackets), and the minimum and
914 maximum value of each distribution.
915

916 Figure 4. Distribution of AOD at 550 nm over East Asia retrieved from ECMWF for (a) and (e) dust,
917 (b) and (f) organic matter, (c) and (g) black carbon, and (d) and (h) sulphate aerosol. (a) - (d) refers to
918 8 March 2013. That day is classified as a relatively “low polluted” day over East China. (e) - (h) refers
919 to 10 April 2011 which is classified as a comparably “highly polluted” day over East China.
920

921 Figure 5. Scatter diagram of the linear particle depolarization at 532 nm versus (a), (d) the
922 backscatter-related Ångström exponent (355/532 nm wavelength pair), (b), (e) the lidar ratio at 355
923 nm and (c), (f) the lidar ratio at 532 nm. The left column (a-c) shows the optical properties of Asian
924 dust layers considered as less polluted (LP), the right column (d-f) shows the more polluted cases.
925

926 Figure 6. (top panel) Transport pattern of the dust plumes that originated in the desert regions and
927 passed over industrialized/populated regions of China before arrival over the Korean peninsula.
928 (middle panel) Vertical position of the dust layers during transport: (a) Dust layers passed over China
929 at high altitude (Case I) (b) dust layers were transported over China through the near surface/lower
930 troposphere (Case II). (bottom panel) Scatter diagram of the linear particle depolarization at 532 nm
931 versus (c) the backscatter-related Ångström exponent (355/532 nm wavelength pair), and the (d), (e)
932 lidar ratio (at 355 nm and at 532 nm) with respect to Case I and Case II. The two categories I, II are
933 denoted by different colors. Case I is indicated by red circles. Case II is indicated by black circles.
934

935

936 Figure 7. Scatter diagram of the linear particle depolarization at 532 nm versus (a), (d) the
937 backscatter-related Ångström exponent (355/532 nm wavelength pair), (b), (e) the lidar ratio at 355
938 nm and (c), (f) the lidar ratio at 532 nm. The left column (a-c) shows the optical properties of Asian
939 dust layers considered as less polluted (LP), the right column (d-f) shows the more polluted cases. The
940 Asian dust layers that passed over polluted regions in China at low altitude are denoted by black
941 circles. The Asian dust layers transported at high altitude are denoted by red squares.
942

943 Figure 8. (top panel) (a) transport path and classification of East Asian dust layers with respect to (b)
944 their altitude above ground when they passed over industrial regions of China. (bottom panel)
945 transport path and corresponding altitude of Asian dust layers are distinguished by color. (black: 0 km
946 – 1 km; green: 1 km – 2 km; purple: 2 km – 3 km; blue: 3 km – 4 km; red: above 4 km). Scatter plots

947 of the linear particle depolarization at 532 nm (dark yellow), the backscatter-related Ångström
948 exponent (355/532 nm wavelength pair, red), the lidar ratio at 355 nm (blue), the lidar ratio at 532 nm
949 (green) in dependence of the 5 altitude categories (c). The height of the Asian dust layers above
950 ground is separated by vertical lines. Case I included the layers from 3 – 4 km and above 4 km. Case
951 II includes the layers from 0 - 1 km, from 1-2 km, and from 2-3 km height above ground.

952
953 Figure 9. Scatter diagram of optical dust properties versus the time the Asian dust layers travelled over
954 polluted regions in China. Shown are (a) the particle depolarization ratio, (b) the backscatter-related
955 Ångström exponent (355/532 nm wavelength pair), (c) the lidar ratio at 355 nm, and (d) the lidar ratio
956 at 532 nm with respect to their altitude above ground when they passed over industrial regions of
957 China. The corresponding altitude of Asian dust layer are distinguished by color. (black: below 0 km;
958 green: 1 km – 2km; purple: 2km – 3 km; blue: 3 km – 4 km; red: above 4 km)

959
960
961
962
963
964
965
966
967
968
969
970
971
972
973
974
975
976
977

978 Tables

979 [1]

Classification	Number of observed layers	δ_p	S [sr]		\dot{A}_β	
			355 nm	532 nm		
Pollution level ^(a)	Less Polluted	25	0.17±0.02	57±7	55±7	0.82±0.37
	More Polluted	13	0.17±0.02	58±6	59±8	0.89±0.38
Vertical position ^(b)	Case I	16	0.21±0.06	52±7	53±8	0.74±0.31
	Case II	22	0.13±0.04	63±9	62±8	0.98±0.35
Pollution level & Vertical position ^(c)	LP_below 3 km	12	0.13±0.03	64±9	62±8	1.00±0.38
	LP_above 3 km	13	0.21±0.05	51±8	49±9	0.65±0.20
	MP_below 3 km	8	0.13±0.04	61±10	64±7	1.09±0.30
	MP_above 3 km	5	0.24±0.05	53±5	53±2	0.58±0.14

980

981 [2]

Height of dust layer at pollution regions	Number of observed layers	δ_p	S [sr]		\dot{A}_β	
			355nm	532nm		
Case I	Above 4 km	14	0.23±0.02	50±7	49±8	0.60±0.27
	3 km-4 km	1	0.20±0.04	44±2	47±7	0.67±0.29
Case II	2 km-3 km	7	0.13±0.02	61±7	66±5	1.11±0.47
	1 km-2 km	6	0.15±0.03	65±7	59±9	0.94±0.42
	Below 1 km	10	0.12±0.01	63±7	64±6	1.00±0.43

982

983

984

985

986

987

988

989

990

991

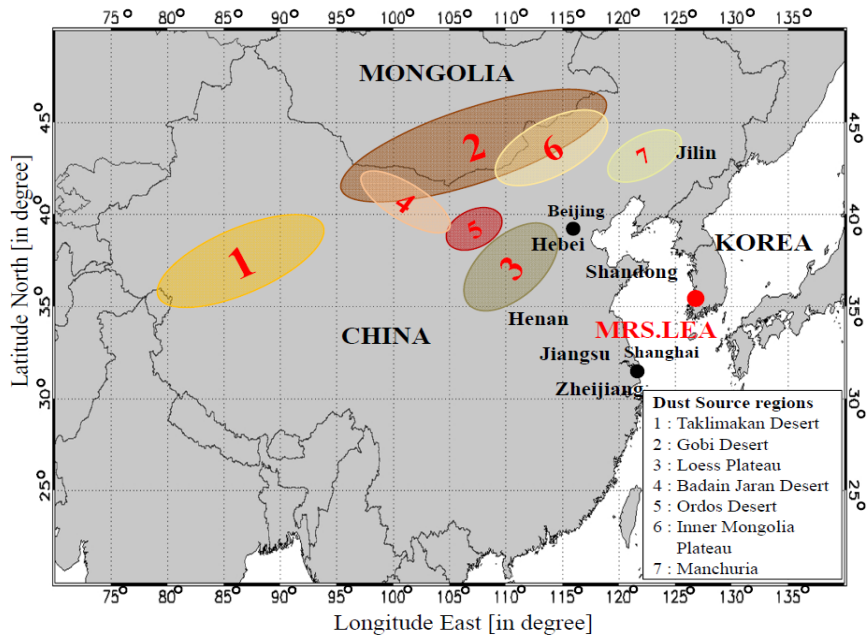
992

993

994

995 Figures

996 [1]



997

998

999

1000

1001

1002

1003

1004

1005

1006

1007

1008

1009

1010

1011

1012 [2]

1013

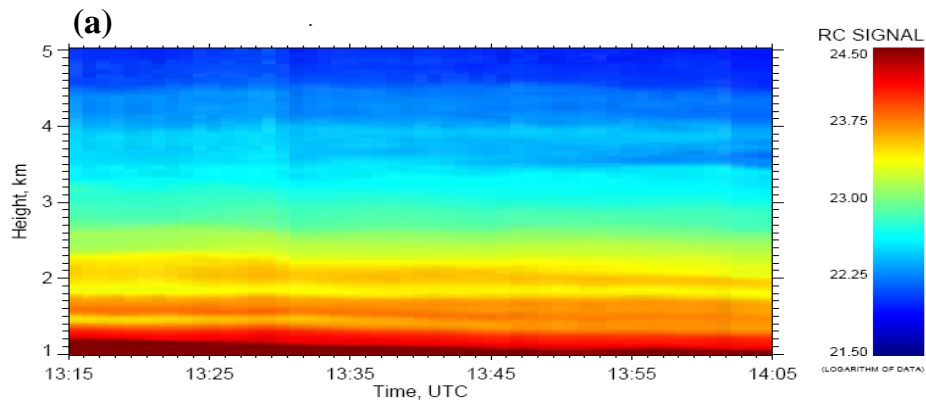
1014

1015

1016

1017

1018



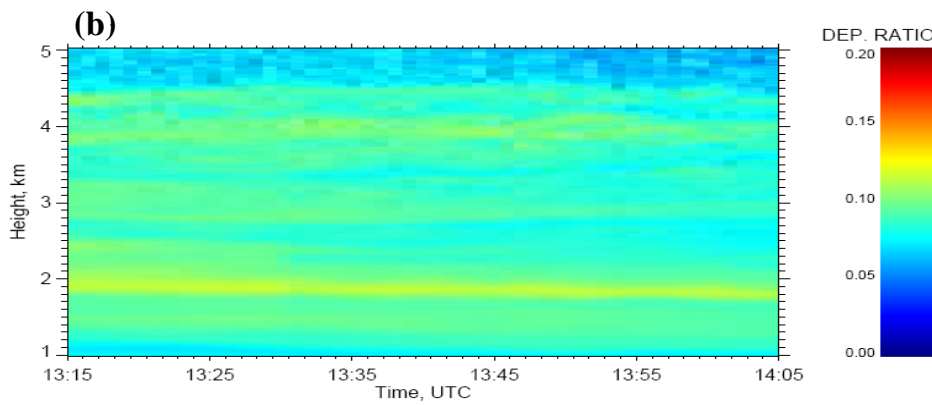
1019

1020

1021

1022

1023



1024

1025

1026

1027

1028

1029

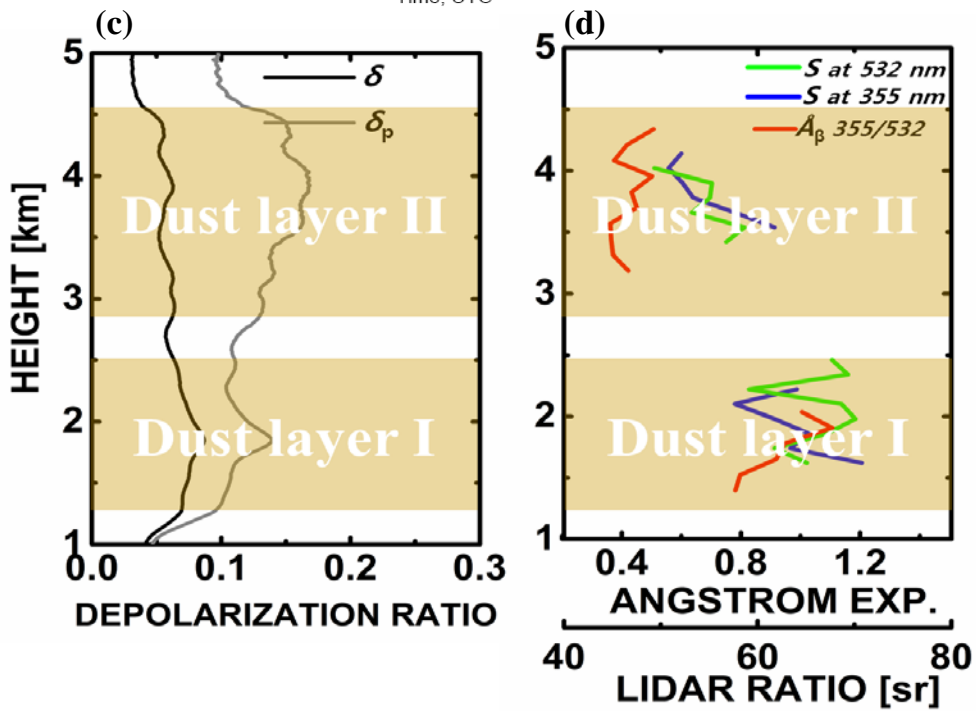
1030

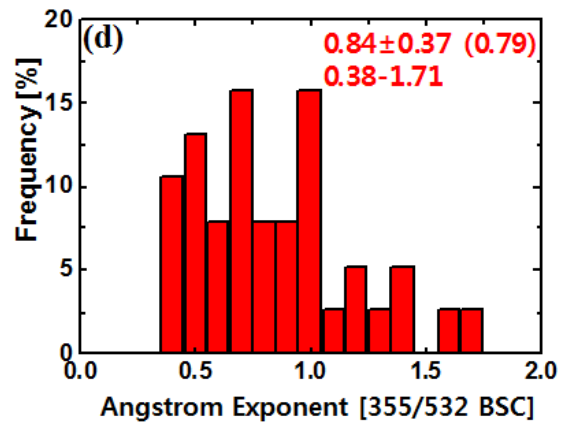
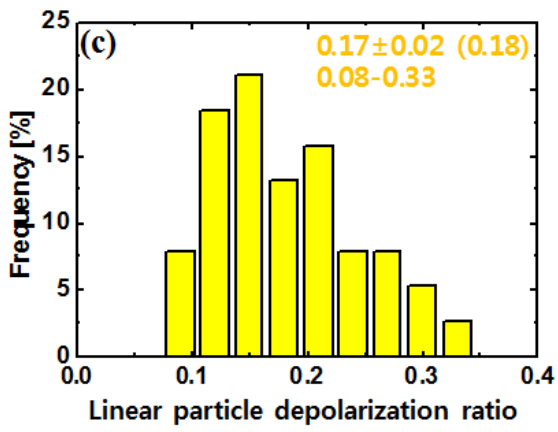
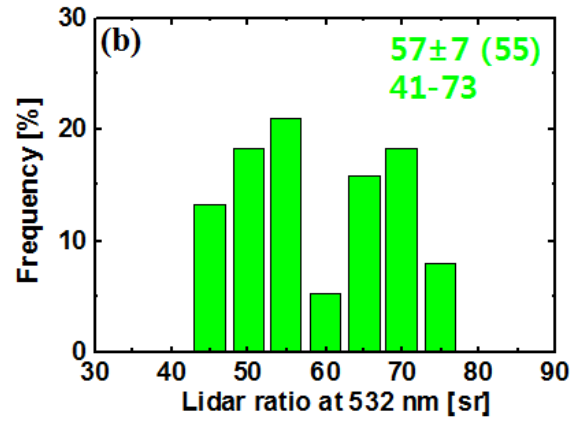
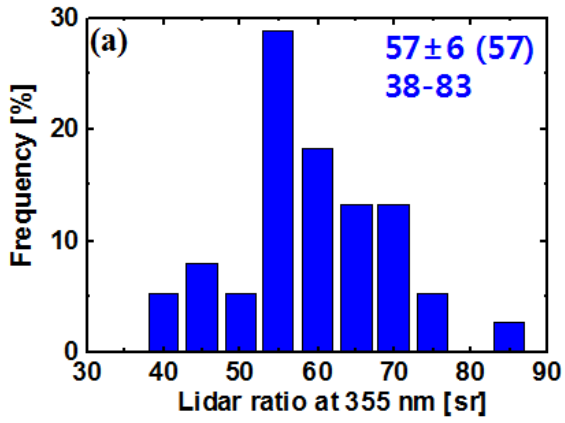
1031

1032

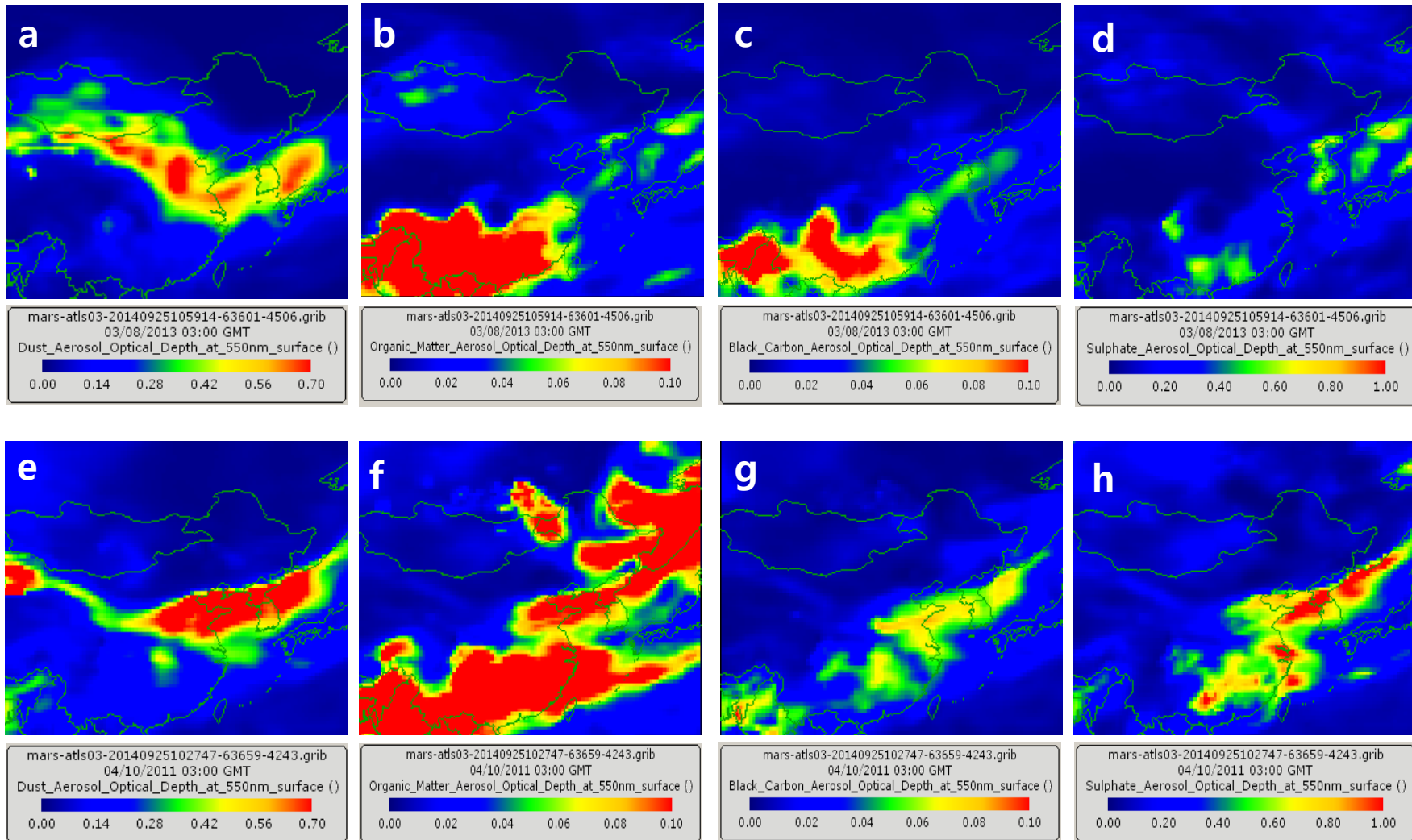
1033

1034

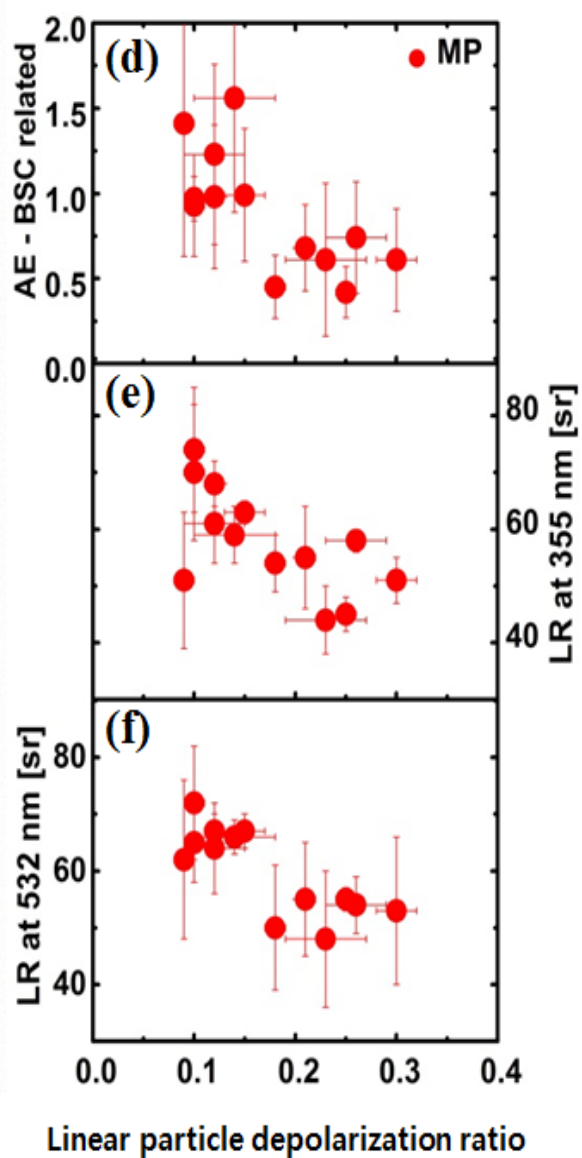
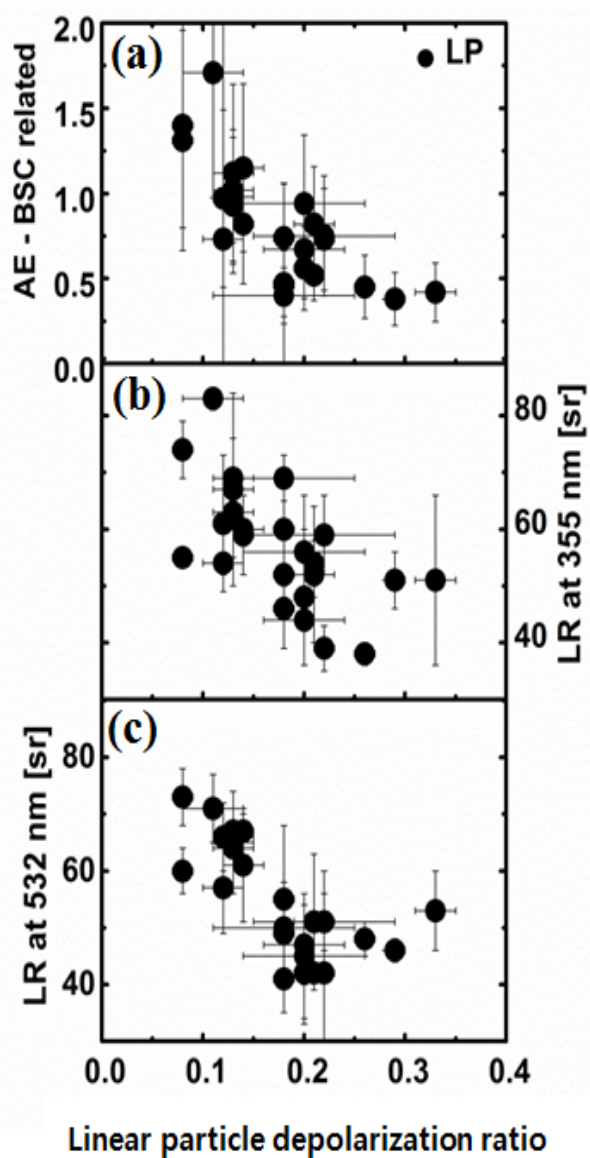




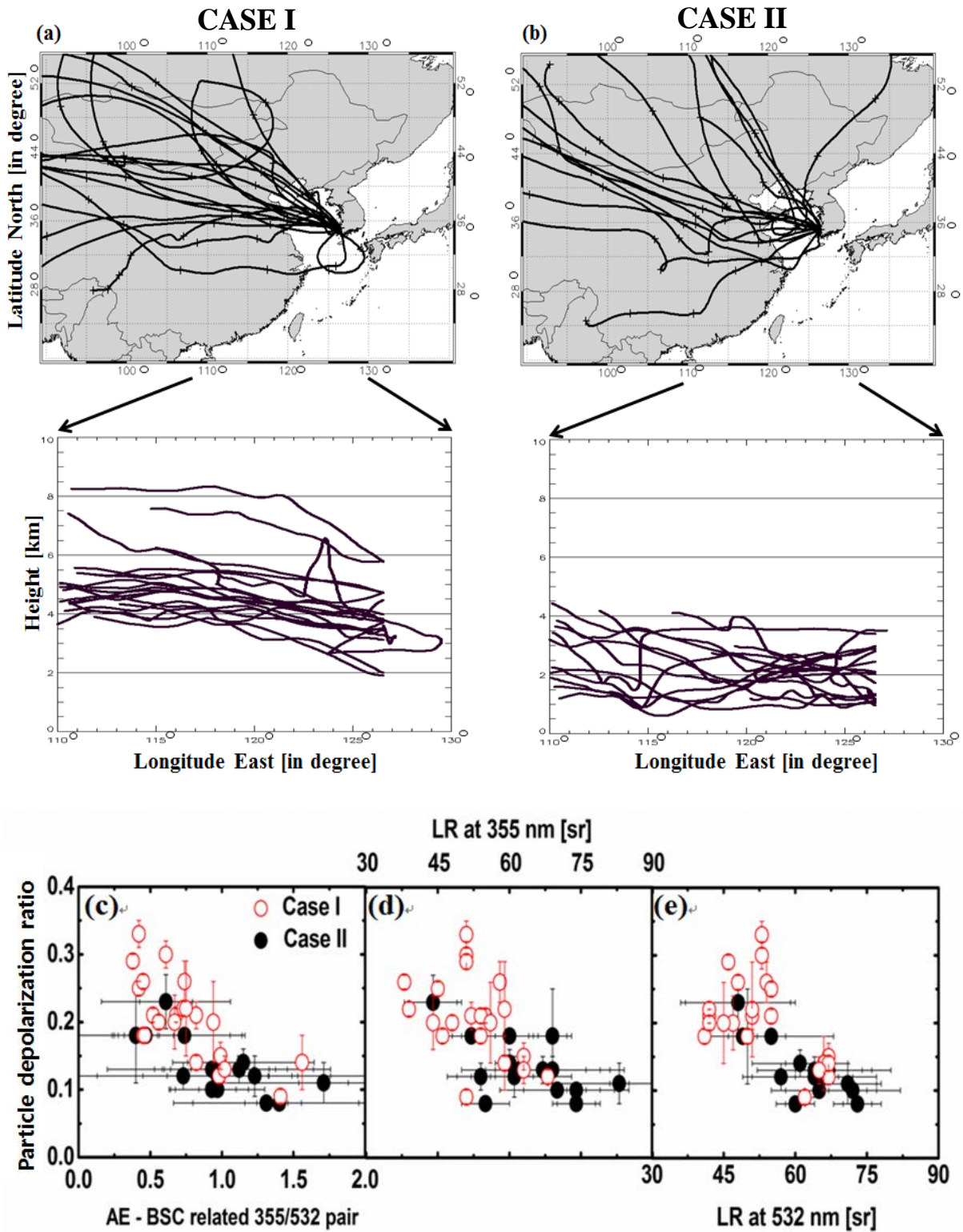
[4]



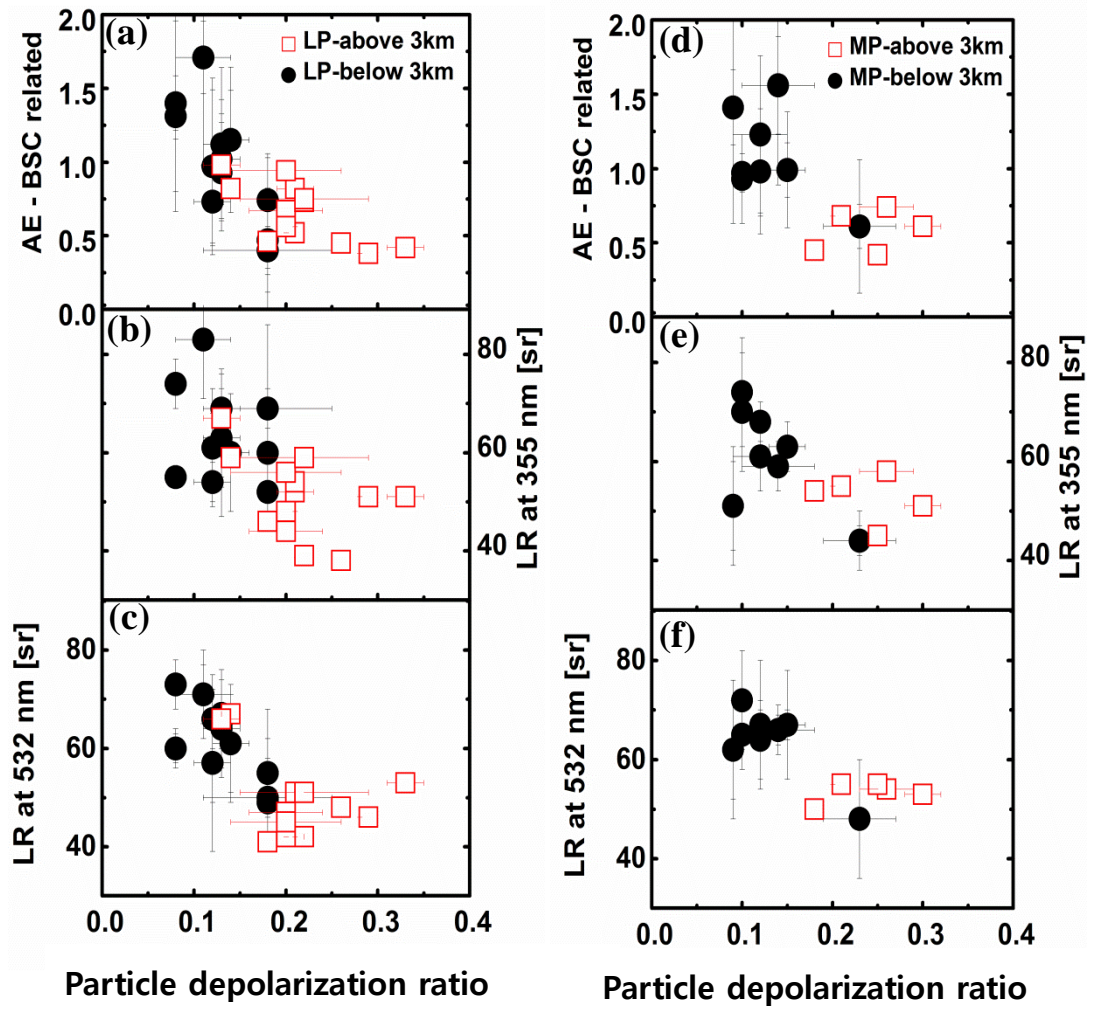
[5]



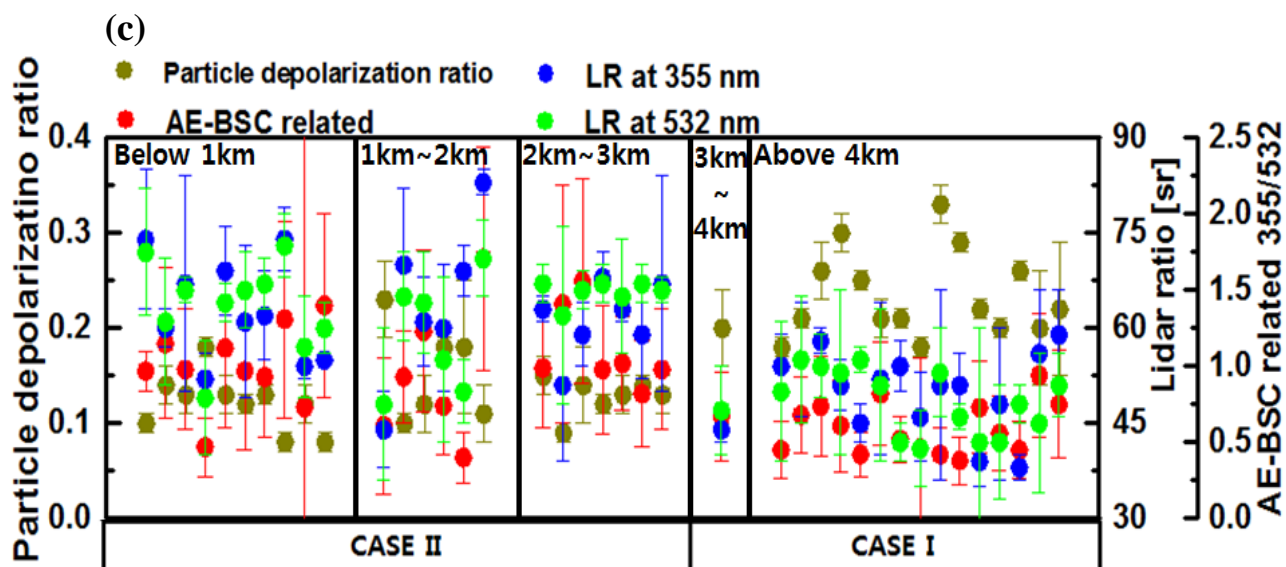
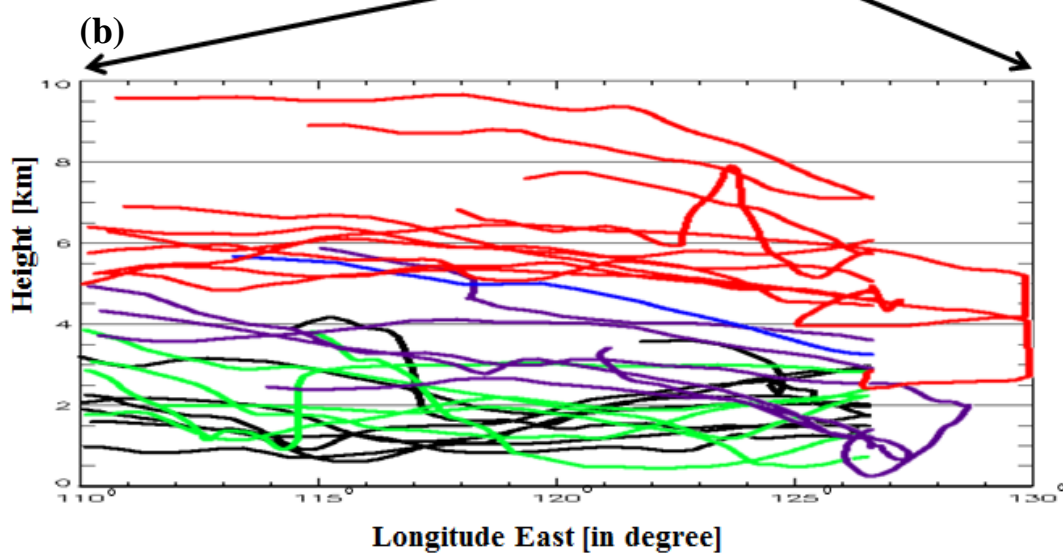
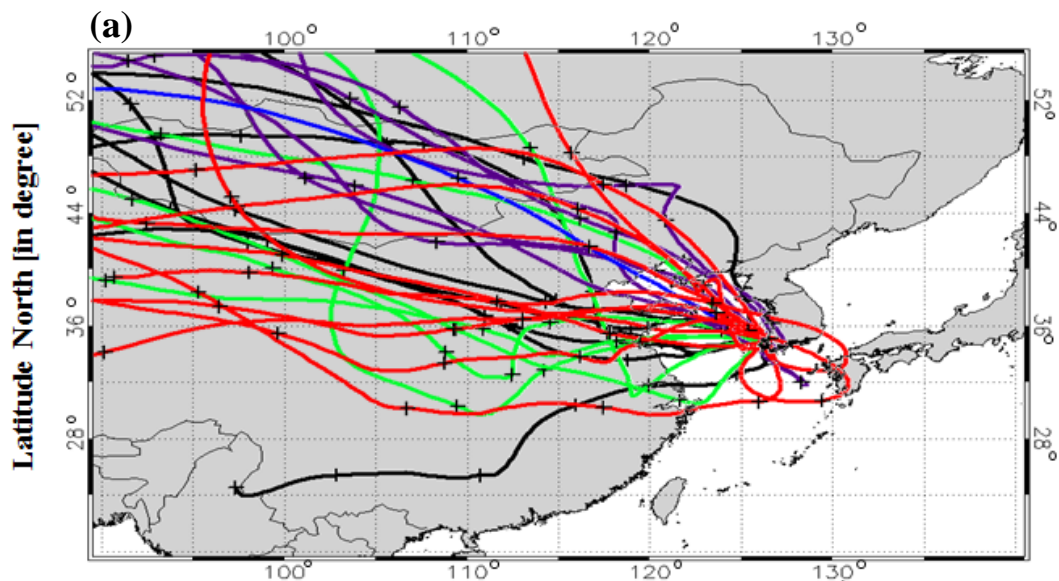
[6]



[7]



[8]



[9]

